Linear magnetoelectric coupling without long-range magnetic order and rare-earth-free large magnetocaloric effect in $Co_3V_2O_8$

S. Mukherjee,[1] N. Mondal,[1] M. Polentarutti,[2] G. Bais,[2] S. Majumdar,[1] and S. Giri[1,*]
[1]*School of Physical Sciences, Indian Association for the Cultivation of Science, Jadavpur, Kolkata 700032, India*
[2]*Elettra-Sincrotrone Trieste S.C.p.A., Area Science Park Basovizza, 34149 Trieste, Italy*

(Received 15 September 2023; revised 10 November 2023; accepted 3 January 2024; published 22 January 2024)

The cobalt atoms within the crystal structure of $Co_3V_2O_8$ arrange themselves into kagome staircase lattices. Our low-temperature synchrotron diffraction studies confirm a distortion in kagome lattices along the [010] direction associated with the anomalous thermal expansion of the unit cell volume below ∼180 K. At this temperature, a structural transition to a polar *Aba*2 space group from the high-temperature structure is suggested. This transition is further confirmed by Raman spectroscopy and is associated with the ferroelectric order at 180 K (T_{FE}). Below T_{FE}, a significant linear magnetoelectric (ME) coupling is realized despite long-range magnetic order occurring below ∼11 K. Thus, ME coupling is linked to the distortion in the kagome lattice structure formed by the Co atoms. These correlations provide an opportunity for manipulating ME coupling at elevated temperatures. The compound exhibits a highly promising magnetocaloric effect in proximity to its magnetic order, constituting another appealing outcome. This characteristic is interesting for the exploration of rare-earth-free magnetocaloric materials.

DOI: 10.1103/PhysRevB.109.014418

I. INTRODUCTION

Geometrically frustrated arrangements of antiferromagnetically coupled magnetic atoms give rise to a captivating degenerate ground state within the realm of magnetism. A prime example is found in the kagome lattice, composed of interlinked triangles sharing corners between adjacent atoms, wherein antiferromagnetic (AFM) interactions occur. The kagome lattice's exceptional allure arises from its one-of-a-kind geometry, resulting in pronounced magnetic frustration. Typically, magnetic frustration suppresses conventional magnetic order, ultimately giving rise to multiple degenerate magnetic ground states. The AFM Heisenberg interaction manifesting on the kagome lattice leads to remarkable consequences. They include the emergence of intriguing phenomena such as topological flat bands [1], as well as the manifestation of gapped or gapless quantum spin liquids [2–5], spin ice [6,7], and even superconductivity [8,9]. Recent observations have directed special attention towards instances of multiferroic order materializing within kagome lattices [10–13]. These observations beckon the scientific community to consider the potential influence of magnetic frustration in the genesis of ferroelectric order within multiferroic materials [14–18]. In fact, the focus of our current exploration lies in the kagome staircase lattice, which offers fertile ground for testing and materializing multiferroic order

The compound $Co_3V_2O_8$ (referred to as CVO) exhibits a crystalline structure with the *Cmca* space group at room temperature, giving rise to the formation of kagome staircase lattices [19–21]. These lattices are composed of two distinct types of Co^{2+} ions, denoted as Co1 and Co2, as illustrated in Fig. 1(a). The Co atoms are positioned within CoO_6 octahedra with oxygen atoms occupying the corners. An illustrative instance of linking Co1-Co2-Co1-Co2-Co1 networks is depicted in Fig. 1(b), where connections between $Co1O_6$ and $Co2O_6$ octahedra within a single unit cell are shown. Notably, the Co-O-Co bond angles closely approximate 90°, and a ferromagnetic (FM) magnetic ground state having Ising-like behavior has been confirmed below 6.2 K (T_C) with spins pointing along the *a* axis from the neutron diffraction [22,23] and neutron scattering experiment [24,25]. As the temperature rises beyond T_C, a transversely polarized AFM spin density wave (SDW) state emerges. This state is characterized by two propagation vectors, specifically $(0, \delta, 0)$, where δ assumes values of 0.33 and 0.5, occurring below $T_N \approx 11$ K. In light of these findings, a magnetic phase diagram has been postulated which outlines the interplay of quantum phase transitions influenced by magnetic field and temperature [26]. Recent neutron diffraction findings utilizing time-of-flight techniques introduced a novel perspective, suggesting a noncollinear magnetic structure characterized by an unexpectedly substantial Dzyaloshinskii-Moriya interaction within the nearest-neighboring Co-O-Co exchange interaction [27].

Intricate magnetic phase diagrams have been formulated, particularly in response to the application of magnetic fields, and additionally, a commensurate SDW state was proposed with a propagation vector of (0,0.4,0) [28–31]. The influence of magnetic fields on the local lattice configuration was meticulously examined using magnetoinfrared spectroscopy, revealing a pronounced magnetoelastic coupling [32]. Significant negative magnetocapacitance was proposed from the magnetic field driven dielectric permittivity [33]. Intrinsic magnetocrystalline anisotropy due to the presence of Co^{2+} ions, coupled with magnetic field induced spin reorientation,

*sspsg2@iacs.res.in

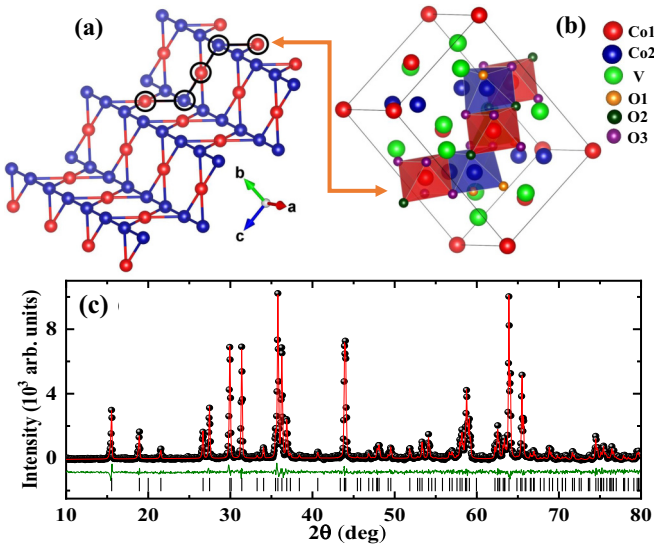

FIG. 1. (a) Kagome staircase lattice consisting of two cobalt atoms. (b) The connecting octahedra within the unit cell. (c) Rietveld refinement of the XRD pattern at room temperature.

was documented through bulk magnetization assessments of CVO crystals [34]. Furthermore, a discernible alteration of the thermal conductivity with magnetic fields was experimentally demonstrated, indicating a substantial heat switch effect [35].

In recent times, the isomorphous compound $Ni_3V_2O_8$ has garnered substantial attention and has been revisited on multiple occasions. This renewed interest stems from its role as a focal point for realizing intricate type-II multiferroic phenomena, closely tied to a complex magnetic phase diagram [14–17]. This magnetic complexity was underscored by an intriguing observation: the manifestation of magnetoelectric (ME) memory effects [18].

In the current investigation, a distinct class of multiferroic order is realized in the case of CVO. Notably, the polarization P reaches remarkably high saturation values, ranging approximately from 0.11 to 0.6 $\mu C/cm^2$, in poling fields spanning 1 to 9 kV/cm. Intriguingly, a linear ME coupling is unveiled below the ferroelectric transition at 180 K, despite the observation that the magnetic order materializes below 11 K. This ME coupling is proposed to be intricately linked to the possible short-range magnetic order, which is instigated by distortions within the kagome staircase lattice structure along the crystallographic b axis. The emergence of ferroelectric order is concurrent with distinctive changes. These encompass steplike distortions within Raman modes and a structural transition from the *Cmca* space group to a polar *Aba*2 structure, which is accompanied by anomalous thermal expansion of the unit cell volume below the structural transition. An impressive magnetocaloric effect (MCE) comes to light, characterized by a substantial entropy change (∼17 J/kg K) associated with a maximum temperature shift of 11.2 K, which is influenced by an application of a 50 kOe magnetic field. Notably, the magnetic refrigeration capacity proves to be considerable at around 300 J/kg, rendering it particularly promising within the realm of rare-earth-free oxides.

II. EXPERIMENTAL DETAILS

Polycrystalline $Co_3V_2O_8$ was synthesized using a standard solid-state reaction technique [36]. The single-phase chemical composition of this sample was confirmed by the x-ray diffraction (XRD) studies at room temperature using a PANalytical x-ray diffractometer (model: X'Pert PRO) with Cu $K\alpha$ radiation. Low-temperature synchrotron diffraction studies were carried out at the Eletra XRD-1 synchrotron facility, Trieste, Italy, with a wavelength of $\lambda = 0.7762$ Å from 300 down to 80 K. The diffraction data were analyzed using the Rietveld refinement procedure with the commercially available open-source software MAUD (Material Analysis Using Diffraction). A thin layer of the pelletized sample was used for the pyroelectric measurements. In all measurements, the electrical contacts were made using silver paint. The pyroelectric current I_p was recorded using an electrometer (Keithley, model 6517B) coupled with a commercial PPMS-II Evercool system from Quantum Design. The poling electric fields were applied during the cooling process. At the lowest temperature both ends of the electrical connections were short-circuited for an adequately long time. The pyrocurrent I_p was then measured during the heating process at a constant temperature-sweep rate. The dielectric measurements was carried out using an E4980A LCR meter (Agilent Technologies, United States) equipped with the same PPMS-II system. The specific heat measurements were done using a PPMS DynaCool system by Quantum Design. Magnetization was recorded using a vibrating sample magnetometer by Quantum Design (Evercool). Temperature-dependent Raman spectroscopy measurements were carried out using a Horiba T6400 Raman spectrometer (excitation wavelength = 532 nm with a spot size of 1 μm).

III. EXPERIMENTAL RESULTS AND DISCUSSION

A. Room temperature x-ray diffraction

The XRD pattern at 300 K is shown in Fig. 1(c). The Rietveld refinement was satisfactorily conducted utilizing the *Cmca* space group, as shown by the solid curve. The lower portion displays the difference plot, confirming the absence of any impurity phases. The diffraction pattern is refined with coordinates Co1(0, 0, 0), Co2(1/4, 0.1264(7), 1/4), V(0, 0.3793(7), 0.1137(8)), O1(0, 0.2433(8), 0.2326(8)), O2(0, −0.0013(8), 0.2422(6)), and O3(0.2898(8), 0.1225(9), 0.9794(7)). The refined lattice constants are $a = 5.9356(7)$, $b = 11.3901(2)$, and $c = 8.2351(3)$ Å with reasonable reliability parameters; $R_w(\%) \sim 3.07$, $R_{exp}(\%) \sim 0.81$, and $\chi^2 \sim 1.48$. The values of the lattice constants are consistent with previously reported results [36].

B. Magnetization and magnetocaloric effect

Thermal variation of magnetization M is recorded in the zero-field-cooled (ZFC) mode, displaying different characteristic features at low temperature T, which is shown in Fig 2(a). The low-T results are magnified in the inset. Three magnetic transitions are observed in the ZFC magnetization with decreasing temperature around ∼11, ∼6.5, and ∼5.9 K, which correspond to a paramagnetic to high-T incommensurate (IC) AFM transition (T_N^{II}), a high-T IC AFM to a low-T IC AFM

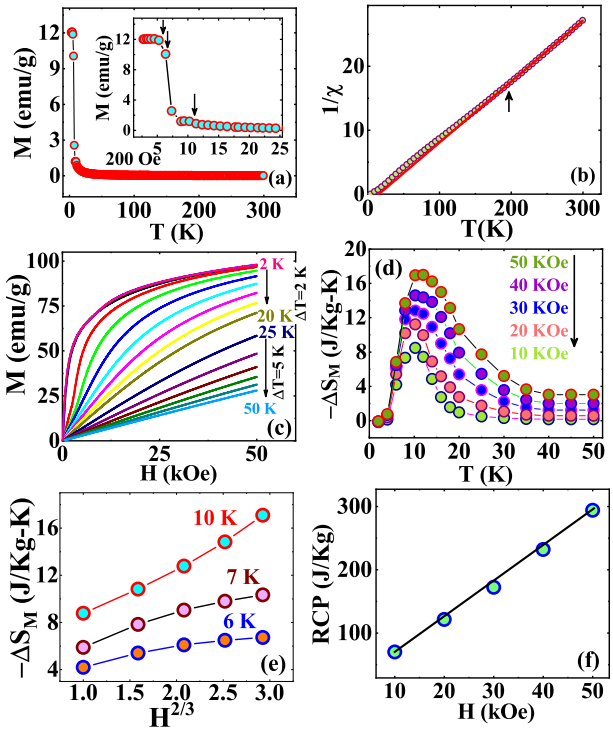

FIG. 2. (a) Thermal variation of magnetization at 200 Oe. The inset magnifies the low-T curve, highlighting three magnetic transitions with arrows. (b) Curie-Weiss fit of the inverse susceptibility. The arrow indicates the temperature below which it deviates from Curie-Weiss behavior. (c) Magnetization curves at regular intervals of temperatures. (d) Magnetic entropy change ΔS_M, as obtained from the magnetization isotherms, with T for the selected ΔH. (e) Plot of ΔS_M with $H^{2/3}$ at 10, 7, and 6 K. (f) Magnetic field variation of RCP.

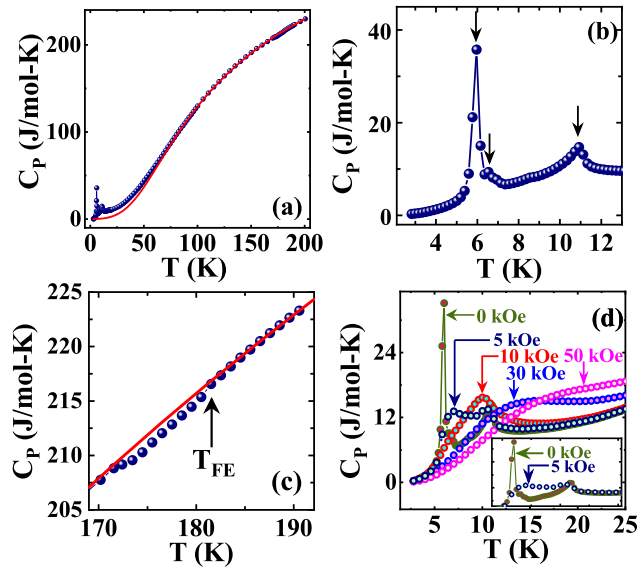

FIG. 3. Thermal variation of specific heat (a) from 2 to 300 K, where the solid curve shows the calculated value using the Debye-Einstein model, as described in the text, (b) in the low-temperature range, highlighting three transitions, (c) close to T_{FE}, and (d) low-temperature results at different magnetic fields. The inset of (d) magnifies the results for $H = 0$ and 5 kOe.

transition (T_N^{I}), and a low-T IC AFM to FM transition (T_C), respectively, in accordance with previous reports [22,23,26]. These three magnetic transitions are also evident in the heat capacity C_P results, as depicted in Fig. 3(b). Thermal variation of the inverse susceptibility χ^{-1} is shown in Fig. 2(b). The Curie-Weiss fit is shown by the straight line, which deviates from the linearity below ~200 K, as indicated by the arrow. The fit indicates the values of the Curie-Weiss temperature Θ and effective paramagnetic moment μ_{eff} are ~15 K and 5.28 μ_B. The value of μ_{eff} is considerably higher than the theoretical spin-only value (3.87μ_B) and lower than the theoretical value (6.63μ_B) of Co^{2+} considering spin and orbital contributions. The results confirm a significant contribution from the orbital component to μ_{eff}.

Isothermal magnetization curves are recorded at selected T, which are shown in Fig. 2(c) for a T range of 2–60 K. The low-T curves show a saturating trend close to 50 kOe. Importantly, the magnetization curves are nonlinear to ~40 K, which is much higher than T_N^{II}, pointing to a dominant short-range magnetic order. The change in entropy ΔS_M is calculated from the magnetization curves using the formula $\Delta S_M(H,T) = \int_0^H [dM(H,T)/dT]_H dH$, which is derived by employing Maxwell's equations. Thermal variations of ΔS_M for a selected range of field change ΔH are shown in Fig. 2(d). ΔS_M emerges below ~40 K and exhibits a maximum close to T_N^{II}. The value of $|\Delta S_M|$ is as high as 17 J/kg K for $\Delta H = 50$ kOe, which is promising, as the MCE is realized without a contribution from the rare-earth (R) moments. The H dependence of $-\Delta S_M$ at the magnetic order may provide the nature of the magnetic order, which has been investigated both experimentally [37–39] and theoretically using a mean-field approach [40]. According to the mean-field approximation, ΔS_M can be expressed as $\Delta S_M \propto H^n$ with an exponent $n = 2/3$ at the magnetic order. The above relation does not hold close to T_C, T_N^{I}, and T_N^{II}, as depicted in Fig. 2(e). The discrepancy was explained recently [41] on the basis of Landau's theory of second-order phase transitions [42], which was applied to the spatially inhomogeneous ferromagnets. The magnetic refrigeration capacity (RCP) is defined as $|\Delta S_M|_{\max} \times$ FWHM, which can be estimated from the ΔS_M vs T plot. $|\Delta S_M|_{\max}$ is the maximum value of $|\Delta S_M|$, and FWHM is the full width at half maximum of the ΔS_M vs T plot. The value of RCP is plotted with H, which increases almost linearly, as indicated by the straight line in Fig. 2(f). The value of RCP is considerable at ~300 J/kg for $\Delta H = 50$ kOe.

C. Heat capacity and magnetic entropy

Heat capacity C_P is recorded with T in zero field and at selected H. Figure 3(a) exhibits the thermal variation of C_P in zero field. A trial of the fitting of the high-temperature $C_P(T)$ data is initiated with the standard Debye law, which is unsuccessful. However, the $C_P(T)$ curve satisfactorily fits the Debye-Einstein model [43–47], $C_P(T) = pD(\theta_D, T) + (1-p)E(\theta_E, T) + \gamma T$, with Debye temperature $\theta_D = 360$ K, Einstein temperature $\theta_E = 790$ K, $\gamma = 0.02$ J/mol K^2, and $p = 0.75$. Here, $D(\theta_D, T)$ and $E(\theta_E, T)$ are the Debye and Einstein functions, respectively. The fitted curve is shown by

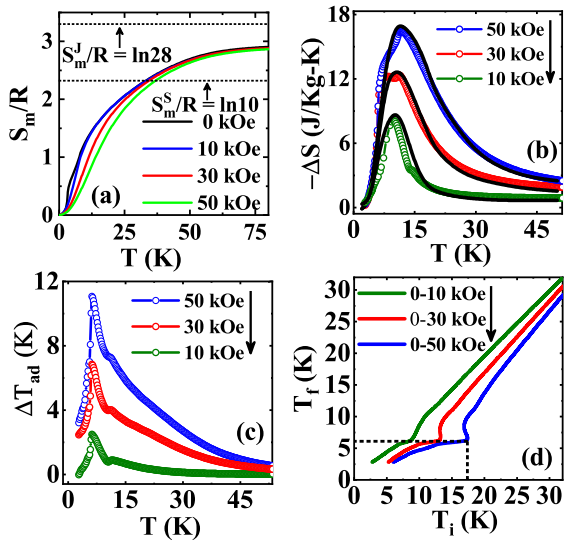

FIG. 4. T variation of (a) magnetic entropy, (b) ΔS_M as obtained from C_P (symbols) and compared with the same obtained from magnetic isotherms (solid lines), and (c) adiabatic temperature change ΔT_{ad} and (d) plot of the final temperature T_f against the initial temperature T_i for different ΔH.

the solid line in Fig. 3(a). The low-T results are magnified in Fig. 3(b), with three arrows at T_C, $T_N^{\rm I}$, and $T_N^{\rm II}$ with increasing T, which is consistent with the magnetization results. The high-T region of $C_P(T)$ is further magnified in Fig. 3(c). The arrow indicates the ferroelectric ordering temperature $T_{\rm FE}$, around which the $C_P(T)$ data deviate from the fit using the Debye-Einstein model. The $C_P(T)$ data are also recorded for selected H. The low-T $C_P(T)$ results are highlighted in Fig. 3(d), showing different characteristic features for different H. The inset magnifies the features of low-T $C_P(T)$ for $H = 0$ and 5 kOe. The sharp peak at T_C in zero field nearly vanishes at $H = 5$ kOe, pointing to a huge low-H ($\leqslant$5 kOe) magnetocaloric effect around T_C. The shoulderlike anomaly at $T_N^{\rm I}$ modifies to a broadened maximum, whereas the intensity of the broadened maximum at $T_N^{\rm II}$ slightly decreases and shifts towards lower temperature. The broadened maximum around $T_N^{\rm I}$ almost disappears at 10 kOe, whereas the intensity of the anomaly around $T_N^{\rm II}$ increases and shifts towards lower temperature. At high H, the maximum smears out and shifts in the opposite direction towards higher temperature.

The lattice heat capacity data, as calculated from a combined Debye and Einstein model, is subtracted from the experimental $C_P(T)$ data to calculate the magnetic contribution C_m. The magnetic entropy S_m is thus obtained by integrating $(C_m/T)dT$. Since the $C_P(T)$ data are not available below 2.5 K, the entropy change is determined by interpolating the $C_P(T)$ curves between 0 and 2.5 K using the standard methods [48]. The fully saturated value scaled with $R = 8.31$ J/mol K is shown by the dashed lines in Fig. 4(a) by taking into account of the spin-only value of $\ln(2S + 1)$ and by adding the orbital contribution $\ln(2J + 1)$ of Co^{2+}. S_m/R shows a saturating trend above ~52 K. The saturated experimental value is found to be close to the middle of the fully saturated theoretical values, which suggests a significant contribution from the orbital moment to the overall magnetic entropy.

TABLE I. Values of $-\Delta S_M$, ΔT_{ad}, and the transition temperature T_C/T_N for CVO along with previously reported promising oxides.

Compound	$-\Delta S_M$ (J/kg K)	ΔT_{ad} (K)	H (kOe)	T_C/T_N (K)	RCP (J/kg)
$Co_3V_2O_8$[a]	17	11.2	50	11	300
$GdAlO_3$[b][56]	22	4.5	50	4	77
$DyVO_4$[b][57]	19	12	50	10	325

[a]This work.
[b]Rare earth based.

To compare the magnetic entropy change as estimated from the magnetization isotherms, $\Delta S_M(T)$ is also calculated from the $C_P(T)$ data in field using $\Delta S_M = \int_0^T [C_P(H_2, T) - C_P(H_1, T)]/T dT$, where $C_P(H, T)$ is the heat capacity as a function of H and T. The solid curves in Fig. 4(b) show ΔS_M with T for selected ΔH and are compared with the values of ΔS_M (symbols), as obtained from the magnetization isotherms. The values of $\Delta S_M(T)$ nearly match, and the small difference might be attributed to the underestimation of the magnetic heat capacity. Magnetic refrigeration is tested by calculating the adiabatic temperature change ΔT_{ad}. The isentropic change in temperature between the entropy curves $S(H, T)$ and $S(0, T)$ provides the value of ΔT_{ad} [49]. Figure 4(c) shows the T dependence of ΔT_{ad} for different ΔH. The maximum value of ΔT_{ad} is observed to be ~11.3 K around 7 K, which is significant for a moderate change in ΔH of 50 kOe. We note an asymmetry in the $\Delta T_{ad}(T)$ curve at about 10 K when applying a field adiabatically (ΔT_{ad} heating) and removing the field adiabatically (ΔT_{ad} cooling). The cooling effect attributed to the adiabatic removal of magnetic field can be realized for the selected ΔH. The final temperature T_f can be obtained by adiabatic demagnetization from an initial temperature T_i. The plots of T_f vs T_i for selected ΔH are depicted in Fig. 4(d). For example, the dashed lines demonstrate that T_i around 17.4 K is reduced to ~6.4 K for $\Delta H = 50$ kOe, which is a huge change and comparable to the results of promising compounds [50,51].

Another captivating finding from the ongoing investigation is the substantial magnetocaloric effect observed in a compound free from rare earth elements [52–55]. The current value of $-\Delta S_M$ is high and comparable to what we found in rare-earth-based oxides in a similar temperature range in previous studies, as shown in Table I. The value of ΔT_{ad} is considerable as 11.2 K around 7 K for $\Delta H = 50$ kOe. The value of RCP is significant for CVO. Here, single-ion anisotropy driven by Co^{2+} in CVO contributes to the promising magnetocaloric effect, and the significant contribution from the orbital moment gives rise to the observed large magnetocaloric effect.

D. Dielectric permittivity and magnetodielectric effect

Dielectric permittivity ϵ is measured with T at a particular frequency f, for example, at $f = 2007$ Hz in zero magnetic field. Thermal variations of the real (ϵ') component of ϵ and

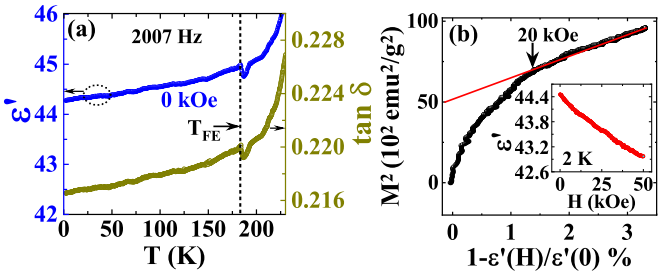

FIG. 5. (a) Thermal variations of the real part ϵ' and dielectric loss $\tan\delta$, indicated on the left and right axes, respectively. (b) Plot of M^2 vs $[1-\epsilon'(H)]/\epsilon'(0)$. The inset shows the field variation of ϵ' at 2 K.

$\tan\delta$ are shown in Fig. 5(a). The evidence of an anomaly at the same temperature (T_{FE}) in ϵ' and $\tan\delta$ primarily indicates the onset of spontaneous polar order [58,59]. ϵ' is recorded with H at 2 K, which is shown in the inset of Fig. 5(b). The percentage of magnetodielectric (MD) response, defined as $[\epsilon'(H)/\epsilon'(H=0)-1]\times 100$, is ∼3.3% for $H = 50$ kOe.

The MD response correlates with the ME coupling, which is phenomenologically expressed using the Ginzburg-Landau theory through the ME coupling term γP^2M^2 in the thermodynamic potential Φ, which is defined as

$$\Phi = \Phi_0 + \alpha P^2 + \frac{\beta}{2}P^4 - PE + \alpha' M^2 + \frac{\beta'}{2}M^4 - MB + \gamma P^2M^2. \quad (1)$$

Here, α, β, α', β', and γ are the constants and functions of temperature. In the magnetically ordered state, the influence of magnetic order on the MD response is followed by a linear response of the M^2 versus MD(%) curve. The M^2 versus MD(%) plot at 2 K is shown in Fig. 5(b). The linearity of the plot holds satisfactorily for $H \geqslant 20$ kOe, as indicated by the arrow. The linearity of the plot indicates that the ME coupling term γP^2M^2 of the Ginzburg-Landau theory is significant for CVO, as reported earlier for different multiferroics [60–66].

E. Ferroelectric order and magnetoelectric coupling

Thermal variations of the pyroelectric current I_p recorded with a poling electric field E of 5 kV/cm and a thermal sweep rate of 5 K/min are measured under different poling conditions. To confirm the peak in $I_p(T)$ appearing due to a genuine occurrence of the polar order, $I_p(T)$ are recorded for different poling temperatures T_{pole}, as shown in Fig. 6(a). T_{pole} are selected above (200 and 250 K) and below (100 and 160 K) the significant temperature, where an anomaly is noted in ϵ' as well as $\tan\delta$. However, for all T_{pole} the peak always appears at 180 K (T_{FE}). Although the peak in I_p is reproduced for $T_{pole} > T_{FE}$, the peak at T_{FE} is weaker for $T_{pole} < T_{FE}$. The magnified peak is shown in Figs. 6(b) and 6(c) for $T_{pole} = 160$ and 100 K, respectively. For $T_{pole} = 250$ K, a sharp increase is observed which appears due to the extrinsic thermally stimulated depolarization currents (TSDCs) [67–69]. This TSDC component disappears for T_{pole} at 200 K. We note that the peak height for T_{pole} at 200 and 250 K remains almost the same at T_{FE}, pointing to a genuine occurrence of the polar order.

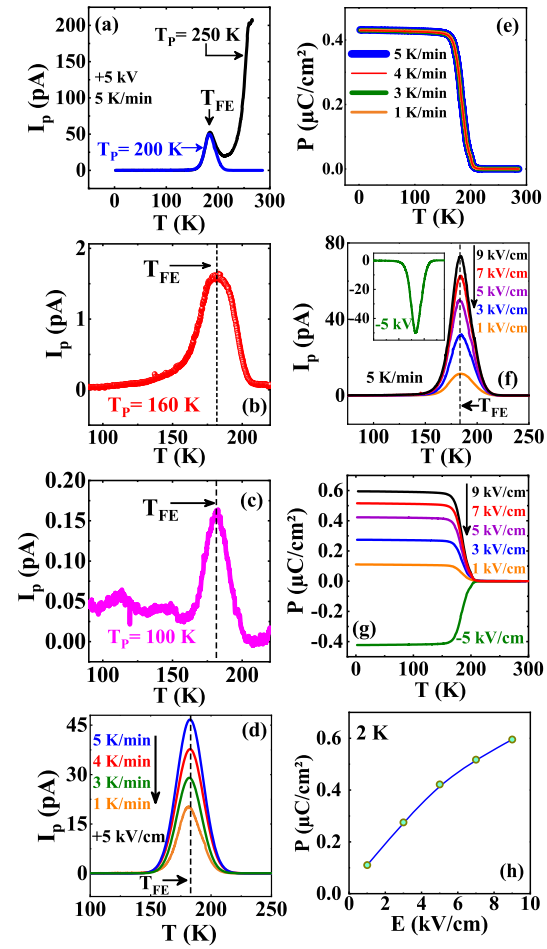

FIG. 6. T variation of (a) I_P at different poling temperatures and magnified I_P near T_{FE} for poling temperatures at (b) 160 K and (c) 100 K with a constant sweep rate of 5 K/min. (d) T variation of I_P at different sweep rates and (e) the corresponding $P(T)$. (f) T variations of I_P at different poling fields E. The inset shows I_P for $E = -5$ kV/cm. (g) $P(T)$ at different E and (h) P vs E.

To further confirm the genuine pyroelectric current around 180 K, $I_p(T)$ is recorded for different thermal sweep rates with a poling field of 5 kV/cm, which is shown in Fig. 6(d). The integration over time provides polarization P as a function of T, as depicted in Fig. 6(e). We note that all the $P(T)$ results nearly merge into a single curve within ∼±0.2% error. $I_p(T)$ is further recorded for different E at a thermal sweep rate of 5 K/min for $T_{pole} = 200$ K. The results are shown in Fig. 6(f). The inset shows $I_p(T)$ for the −5 kV/cm poling field, indicating that the polarization reverses with a negative poling field, suggesting ferroelectric order. $P(T)$ for different E are shown in Fig. 6(g). The values of P with E are shown in Fig. 6(h), which indicates a saturating trend for $E = 9$ kV/cm.

The value of P at 15 K is ∼0.41 μC/cm^2 for a poling field of 5 kV/cm, which is reasonably high with respect to the values for promising multiferroics [13,61,62,70,71]. With application of magnetic field the P value decreases systematically, as shown in Fig. 7(a) and further magnified in Fig. 7(b). The values of P (%) at 3 K are shown with H in Fig. 7(c). The change in P due to 50 kOe magnetic field is ∼3%, which importantly persists well above the nitrogen temperature to

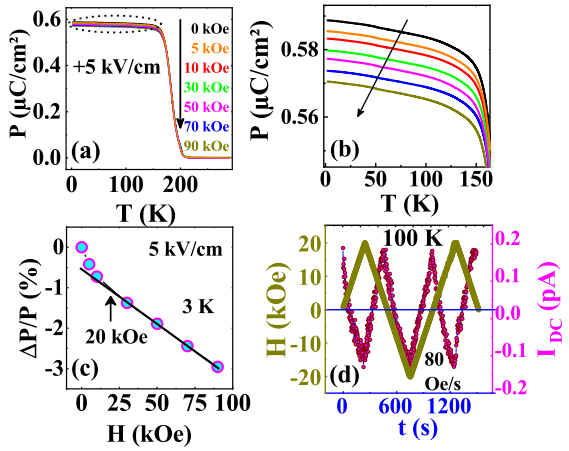

FIG. 7. (a) Thermal variations of P at different magnetic fields H, (b) magnified image of P at different H, (c) plot of $\Delta P/P$ (%) against H at 3 K and 5 kV/cm, and (d) time t dependence of the bias current I_{DC} with $E = +5$ kV/cm and magnetic field H between ± 20 kOe.

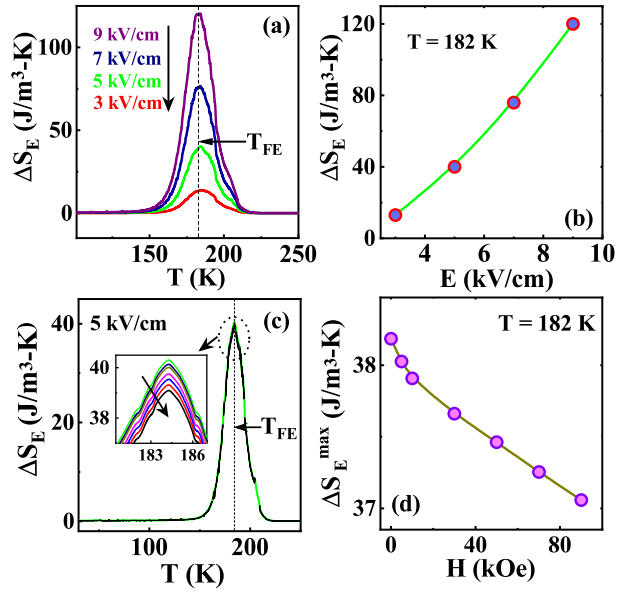

FIG. 8. Thermal variation of (a) ΔS_E at different ΔE and (c) ΔS_E at different ΔH. The inset of (c) highlights the peak region showing the decrease in ΔS_E with increasing H following the change in H for 0, 5, 10, 30, 50, 60, 70, and 90 kOe. (b) ΔS_E with E and (d) ΔS_E with H at 182 K.

$\sim$150 K. The changes in polarization are linear above $\sim$20 kOe, which is consistent with the results observed in the magnetodielectric response. Figure 7(d) demonstrates the change in I_p driven by the change in H between ± 20 kOe with time t at 100 K. To obtain the result the sample was cooled from 200 K with a poling field of 5 kV/cm and cooled through T_{FE} down to 100 K. After temperature was stabilized at 100 K, magnetic field was swiped with a sweep rate of 80 Oe/s, and I_{DC} was simultaneously recorded with t. The changes in I_{DC} with H demonstrate direct observation of ME coupling.

The entropy change ΔS_E with the change in E (ΔE) can be obtained from the Maxwell relation $(\frac{\delta S}{\delta E})_T = (\frac{\delta P}{\delta T})_E$ using $\Delta S_E = \frac{1}{\rho}\int_{E1}^{E2}(\frac{\delta P}{\delta T})_E dE$, where ρ is the mass density [72]. $E1$ and $E2$ are the initial and final electric fields, respectively. Thermal variations of ΔS_E are depicted in Fig. 8(a) for selected values of ΔE. The maximum value of ΔS_E (ΔS_E^{max}) is found to be as high as 120 J/m^3 K at T_{FE} for $\Delta E = 9$ kV/cm. The value of ΔS_E^{max} is considerable and found to be significantly higher than the values of $CoCr_2S_4$ [73], $CaBaCo_4O_7$ [74], and Y_2CoMnO_6 [75]. A plot of ΔS_E^{max} with the change in E at T_{FE} is shown in Fig. 8(b), exhibiting a nonlinear response. The influence of H on ΔS_E is recorded for a poling field of 5 kV/cm, which is depicted in Fig. 8(c). The change in ΔS_E close to T_{FE} is further magnified in the inset. The decrease in ΔS_E^{max} with H at 180 K is depicted in Fig. 8(d), which has a very similar H dependence of P.

F. Temperature-dependent Raman spectra

The orthorhombic structure of CVO consists of edge-sharing CoO_6 octahedra, as depicted in Fig. 1(b), and VO_4 tetrahedra. There are 78 normal modes in CVO, which can be represented by 78 nondegenerate irreducible representations ($\Gamma = 10A_g + 8B_{1g} + 7B_{2g} + 11B_{3g} + 8A_u + 13B_{1u} + 12B_{2u} + 9B_{3u}$). Out of 78 modes, 36 are Raman active modes ($10A_g + 8B_{1g} + 7B_{2g} + 11B_{3g}$) [76]. The peaks in the Raman spectra between 500 and 900 cm^{-1} mainly emerge due to the V-O stretching mixed with some Co-O stretching and bending modes. The modes between 200 and 500 cm^{-1} appear due to the O-Co-O and O-V-O bending modes, and the modes below the 200 cm^{-1} appear due to rigid motions of CoO_6 octahedra and VO_4 tetrahedra. The Raman spectra recorded around T_{FE} are highlighted in Fig. 9(a) at selected T and are consistent with previously reported results [77].

We note that two new modes around 617 and 970 cm^{-1} appear below the ferroelectric order, highlighted by the colored background. The emergence of new modes suggests a structural transition to lower symmetry at T_{FE}. The results for selected peaks in the range of 150–290 K are further shown in Figs. 9(b)–9(g). Figures 9(b) and 9(c), 9(d) and 9(e), and 9(f) and 9(g) show the changes in the peak position and FWHM with T for peaks in the range of $\sim$137.20–137.85 cm^{-1}, $\sim$326.50–329.50 cm^{-1}, and $\sim$813.50–814.6 cm^{-1}, respectively. The insets in Figs. 9(b)–9(g) further highlight the details of the intensities with variations of the temperature. Thermal variations of all the peak positions, FWHM, and integrated intensities exhibit a steplike change close to T_{FE}. The integrated peak intensities increase considerably, whereas FWHMs decrease below T_{FE}. The appearance of new modes and the steplike changes in Figs. 9(b)–9(g) suggest a structural transition around T_{FE}.

G. Low-temperature synchrotron diffraction and structural transition at T_{FE}

The structural properties are investigated by recording the synchrotron diffraction patterns in the range of 80–300 K. The diffraction peaks corresponding to the (002) plane at selected temperatures between 170 and 190 K are depicted in Fig. 10(a), where the peak close to T_{FE} is shown by an arrow. The variations of integrated intensities with T are shown in Fig. 10(b), which reveals a sharp minimum at T_{FE}. The result

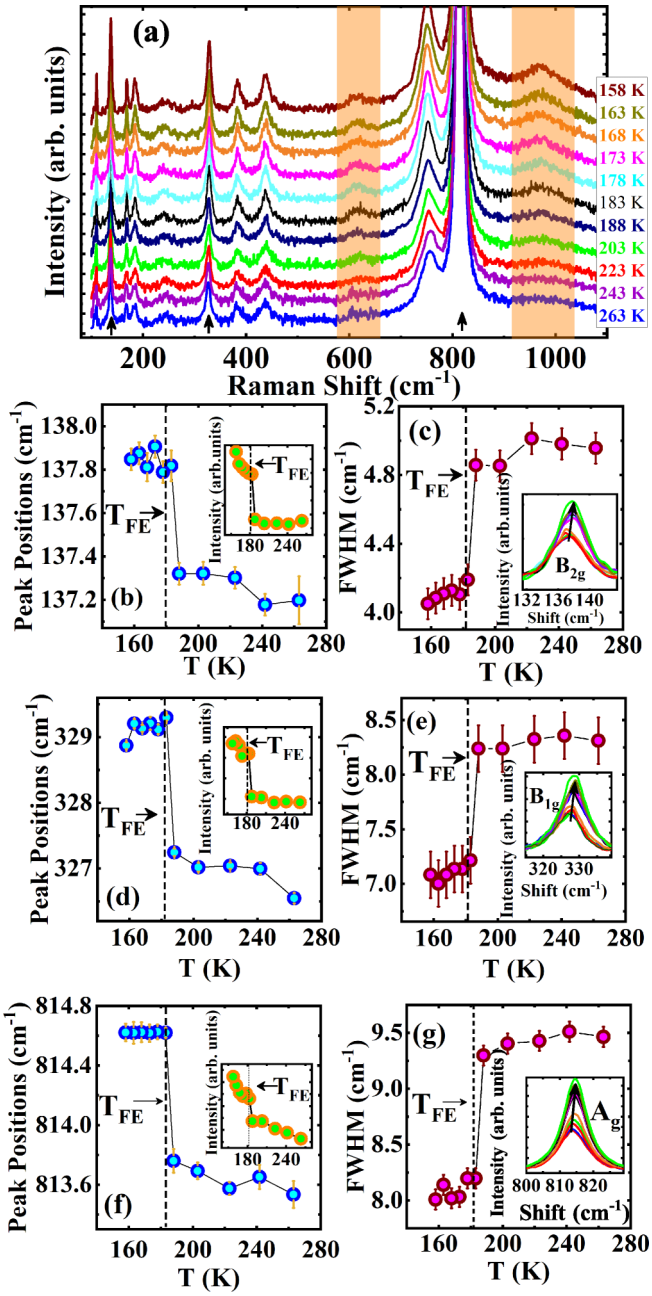

FIG. 9. (a) Raman spectra of CVO at different T. (b), (d), and (f) T variations of Raman peak positions. Insets show the corresponding integrated intensities. (c), (e), and (g) T variation of FWHM. Insets show enlarged individual peaks.

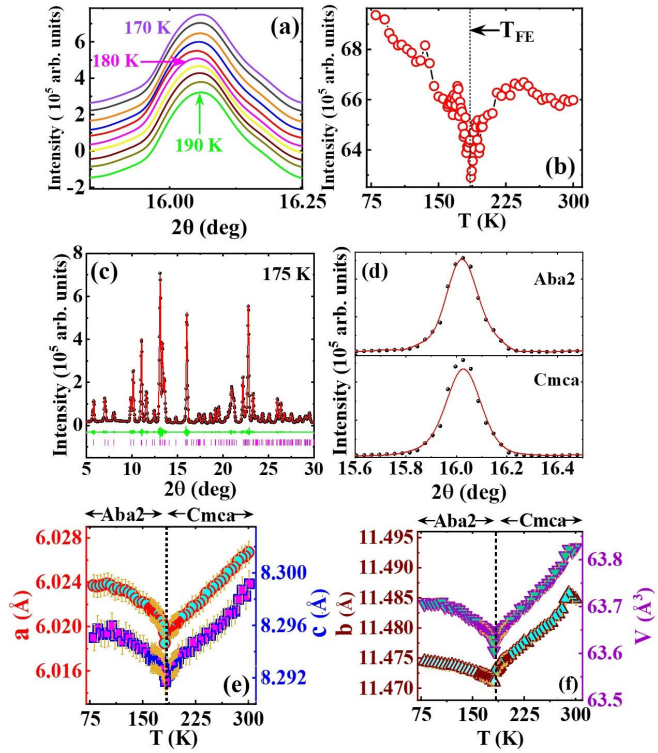

FIG. 10. (a) The peak corresponding to (002) at selected temperatures around T_{FE}. Thermal variations of (b) integrated intensity, (e) lattice parameters a (left axis) and c (right axis), and (f) b (left axis) and V (right axis). (c) Rietveld refinement of the diffraction pattern at 175 K using the *Aba*2 space group. (d) Refinements of a peak around 16° at 175 K (below structural transition) using the *Aba*2 (top) and *Cmca* (bottom) space groups, as indicated by the solid curves.

indicates a change in the scattering cross section around T_{FE} and indicates a possible structural transition, which is consistent with the Raman results. The observed changes in the integrated intensity around T_{FE} are similar to those observed for the multiferroics, involving isostructural changes [60,78] and structural transitions to the lower symmetries [61,79–82]. No new diffraction peak appears below the proposed structural transition, unlike in the Raman results. The diffraction pattern below T_{FE} was refined with the high-temperature *Cmca* (No. 64) space group, which was not satisfactory and indicates a possible structural transition in accordance with the Raman results.

We use the ISODISTORT [83] software to identify a possible structure below the proposed structural transition. We note that the *Aba*2 (No. 41) space group has the highest symmetry among the possible structures. The refinement of the synchrotron diffraction pattern is shown in Fig. 10(c) at 175 K using the *Aba*2 space group. The refined coordinates at 175 K are Co1(0,0,0), Co2 (1/4, 0.1226(6), 1/4), V(0,\break 0.3789(8),0.1129(6)), O1(0,0.2441(7),0.2288(8)), O2 (0,0.0010(6),0.2481(7)), O3 (1/4, 0.1200(8), 0.9791(7)), and O4 (1/4, 0.6250, 0.5250), with the reliability parameters $R_w(\%) \sim 2.25$, $R_{exp}(\%) \sim 0.88$, and $\chi^2 \sim 1.19$. For better clarification, the refinement of a magnified peak around 16° is compared with *Cmca* and *Aba*2 structures in Fig. 10(d). Better refinement of the peak indicates a low-T structure with the *Aba*2 space group. Thermal variations of the lattice constants, a, b, and c, as obtained from the refinements, are depicted in Figs. 10(e) and 10(f). Thermal variation of the unit cell volume V is also shown in Fig. 10(f) on the right axis. All the results exhibit similar characteristic features. With decreasing T the parameters decrease almost linearly until the structural transition at T_{FE}. Below the structural transition they show anomalous thermal expansion until 80 K. The increase in V from T_{FE} to 80 K is 0.15%.

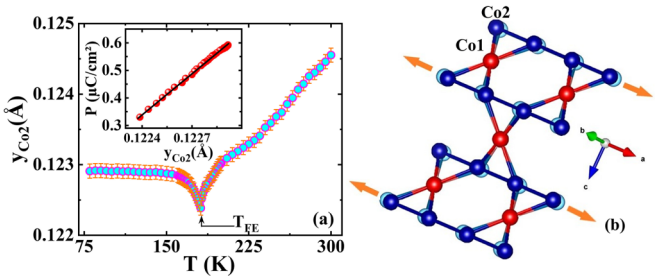

FIG. 11. (a) Thermal variations of the y positions of the Co2 atom; the inset shows the variation of P against the y positions of the Co2 atom. (b) Distortion in the kagome staircase lattice below the structural transition.

H. Magnetoelectric coupling without long-range magnetic order

The transition to a polar $Aba2$ structure at T_{FE} is significant and correlates with the emergence of ferroelectric order. We note that ferroelectric order emerges much higher than the long-range magnetic order. In fact, significant ME coupling has been realized below T_{FE} despite $T_{FE} \gg T_N$ or T_C. In CVO the Co^{2+} ion contributes to only the magnetism, and distortion in the kagome lattice structure formed by Co ions holds the key for ME coupling. Below T_{FE}, the $Aba2$ structure allows two types of Co atoms, such as Co1 and Co2. All the coordinates of Co1 associated with the "x" and "z" coordinates of Co2 are kept fixed during thermal variation, but not the "y" coordinate of Co2. Thus, only the y coordinate of Co2 (y_{Co2}) in the kagome lattice varies with T. Thermal variation of y_{Co2} in the recorded T range is depicted in Fig. 11(a). With decreasing T the magnitude of y_{Co2} decreases, and an increase in y_{Co2} is observed above T_{FE}. The magnitude of y_{Co2} initially increases below T_{FE} and shows a saturating trend below ∼140 K. The inset shows a plot of P with y_{Co2} for selected T below T_{FE}. The solid straight line guides the linearity of the plot and suggests involvement of the distortion in the kagome lattice structure for emerging ferroelectric order. A representation of the distortion in the kagome staircase lattice structure along the [010] direction is depicted in Fig. 11(b). The results further suggest that the deviation from the Curie-Weiss law close to ∼200 K might be involved in the distortion in the kagome staircase lattice structure formed by the Co ions. The crucial insight gleaned from these findings is that the distortion in the kagome lattices driven by Co2 atoms has a correlation with the ME coupling, particularly below T_{FE}. This observation is noteworthy because it represents a relatively rare consequence in the field of multiferroics, shedding light on a novel avenue of exploration in the study of these materials. Further research on single-crystalline CVO (along the crystallographic y axis) is needed to fully understand the implications and mechanisms behind this unique phenomenon. Nevertheless, this work sheds light on the complex interplay between structural, electric, and magnetic degrees of freedom in frustrated magnets and suggests different ways of tuning magnetoelectric coupling at high temperatures.

IV. SUMMARY AND CONCLUSION

In conclusion, the manifestation of ferroelectric order coupled with magnetoelectric effects in CVO is notable, particularly at elevated temperatures. The structural transition towards a polar $Aba2$ structure unequivocally confirms the onset of ferroelectric ordering. Beyond approximately 20 kOe, the linearity of magnetoelectric coupling is substantiated by both polarization and dielectric permittivity responses to magnetic fields. Interestingly, a distinct magnetoelectric coupling emerges below the ferroelectric transition at 180 K, a temperature considerably surpassing the magnetic ordering temperature. The distortion along the [010] direction within the kagome staircase lattice structure correlates with the magnetoelectric coupling below T_{FE}, which is much higher than the long-range magnetic order.

Moreover, a considerable magnetocaloric effect, emerging from the anisotropic magnetic properties of Co ions, becomes conspicuous in close proximity to the magnetic ordering. This feature calls for attention from the scientific community in the pursuit of rare-earth-free materials with promising magnetocaloric properties.

ACKNOWLEDGMENTS

The authors would like to acknowledge Dr. A. Pal and Dr. M. Das for the valuable suggestions. S.G. would like to thank SERB, India, for the CRG project (No. CRG/2022/000718) and the Department of Science and Technology, India, for the financial support (Proposal No. ID-IB-2021-07). The Elettra Synchrotron Facility was funded by a grant (Proposal No. 20195239) from the Italian Ministry of Foreign Affairs and International Cooperation and the Indian Department of Science and Technology.

[1] M. Kang, S. Fang, L. Ye, H. C. Po, J. Denlinger, C. Jozwiak, A. Bostwick, E. Rotenberg, E. Kaxiras, J. G. Checkelsky, and R. Comin, Topological flat bands in frustrated kagome lattice CoSn, Nat. Commun. **11**, 4004 (2020).

[2] S. Maekawa, T. Tohyama, S. E. Barnes, S. Ishihara, W. Koshibae, and G. Khaliullin, *Physics of Transition Metal Oxides* (Springer, Cham, 2004).

[3] T.-H. Han, J. S. Helton, S. Chu, D. G. Nocera, J. A. Rodriguez-Rivera, C. Broholm, and Y. S. Lee, Fractionalized excitations in the spin-liquid state of a kagome-lattice antiferromagnet, Nature (London) **492**, 406 (2012).

[4] S. Yan, D. A. Huse, and S. R. White, Spin-liquid ground state of the S = 1/2 kagome Heisenberg antiferromagnet, Science **332**, 1173 (2011).

[5] S. Depenbrock, I. P. McCulloch, and U. Schollwöck, Nature of the spin-liquid ground state of the $S = 1/2$ Heisenberg model on the kagome lattice, Phys. Rev. Lett. **109**, 067201 (2012).

[6] A. P. Ramirez, A. Hayashi, R. J. Cava, R. Siddharthan, and B. S. Shastry, Zero-point entropy in 'spin ice,' Nature (London) **399**, 333 (1999).

[7] J. Snyder, J. S. Slusky, R. J. Cava, and P. Schiffer, How 'spin ice' freezes, Nature (London) **413**, 48 (2001).

[8] K. Jiang, T. Wu, J.-X. Yin, Z. Wang, M. Z. Hasan, S. D. Wilson, X. Chen, and J. Hu, Kagome superconductors AV_3Sb_5 (A = K, Rb, Cs), Natl. Sci. Rev. **10**, nwac199 (2023).

[9] T. Neupert, M. M. Denner, J.-X. Yin, R. Thomale, and M. Z. Hasan, Charge order and superconductivity in kagome materials, Nat. Phys. **18**, 137 (2022).

[10] K. Yoo, B. Koteswararao, J. Kang, A. Shahee, W. Nam, F. F. Balakirev, V. S. Zapf, N. Harrison, A. Guda, N. Ter-Oganessian, and K. H. Kim, Magnetic field-induced ferroelectricity in S=1/2 kagome staircase compound $PbCu_3TeO_7$, npj Quant. Mater. **3**, 45 (2018).

[11] Y. Li, C. Liu, G.-D. Zhao, T. Hu, and W. Ren, Two-dimensional multiferroics in a breathing kagome lattice, Phys. Rev. B **104**, L060405 (2021).

[12] H. C. Wu, K. Devi Chandrasekhar, J. K. Yuan, J. R. Huang, J.-Y. Lin, H. Berger, and H. D. Yang, Anisotropic spin-flip-induced multiferroic behavior in kagome $Cu_3Bi(SeO_3)_2O_2Cl$, Phys. Rev. B **95**, 125121 (2017).

[13] K. Dey, A. Indra, A. Chatterjee, S. Majumdar, U. Rütt, O. Gutowski, M. v. Zimmermann, and S. Giri, Chemical-pressure-driven orthorhombic distortion and significant enhancement of ferroelectric polarization in $Ca_{1-x}La_xBaCo_4O_7$ ($x \leqslant 0.05$), Phys. Rev. B **96**, 184428 (2017).

[14] G. Lawes, A. B. Harris, T. Kimura, N. Rogado, R. J. Cava, A. Aharony, O. Entin-Wohlman, T. Yildirim, M. Kenzelmann, C. Broholm, and A. P. Ramirez, Magnetically driven ferroelectric order in $Ni_3V_2O_8$, Phys. Rev. Lett. **95**, 087205 (2005).

[15] C. Dong, J. F. Wang, Z. Z. He, Y. T. Chang, M. Y. Shi, Y. R. Song, S. M. Jin, Y. Q. Du, Z. Y. Wu, X. T. Han, K. Kindo, and M. Yang, Reentrant ferroelectric phase induced by a tilting high magnetic field in $Ni_3V_2O_8$, Phys. Rev. B **105**, 024427 (2022).

[16] N. Qureshi, E. Ressouche, A. A. Mukhin, V. Yu. Ivanov, S. N. Barilo, S. V. Shiryaev, and V. Skumryev, Stabilization of multiferroic spin cycloid in $Ni_3V_2O_8$ by light Co doping, Phys. Rev. B **88**, 174412 (2013).

[17] A. Kumarasiri and G. Lawes, Control of the multiferroic transition in $Ni_3V_2O_8$ by transition metal doping, Phys. Rev. B **84**, 064447 (2011).

[18] Y. J. Liu, J. F. Wang, Z. Z. He, C. L. Lu, Z. C. Xia, Z. W. Ouyang, C. B. Liu, R. Chen, A. Matsuo, Y. Kohama, K. Kindo, and M. Tokunaga, Unusual magnetoelectric memory and polarization reversal in the kagome staircase compound $Ni_3V_2O_8$, Phys. Rev. B **97**, 174429 (2018).

[19] N. Rogado, G. Lawes, D. A. Huse, A. P. Ramirez, and R. J. Cava, The kagomé-staircase lattice: Magnetic ordering in $Ni_3V_2O_8$ and $Co_3V_2O_8$, Solid State Commun. **124**, 229 (2002).

[20] G. Balakrishnan, O. A. Petrenko, M. R. Lees, and D. M. K. Paul, Single crystals of the anisotropic kagomé staircase compounds $Ni_3V_2O_8$ and $Co_3V_2O_8$, J. Phys.: Condens. Matter **16**, L347 (2004).

[21] Q. Zhang, W. Knafo, P. Adelmann, P. Schweiss, K. Grube, N. Qureshi, Th. Wolf, H. v. Lohneysen, and C. Meingast, Complex magnetoelastic properties in the frustrated kagome-staircase compounds $(Co_{1-x}Ni_x)_3V_2O_8$, Phys. Rev. B **84**, 184429 (2011).

[22] Y. Chen, J. W. Lynn, Q. Huang, F. M. Woodward, T. Yildirim, G. Lawes, A. P. Ramirez, N. Rogado, R. J. Cava, A. Aharony, O. Entin-Wohlman, and A. B. Harris, Complex magnetic order in the kagomé staircase compound $Co_3V_2O_8$, Phys. Rev. B **74**, 014430 (2006).

[23] N. Qureshi, M. Zbiri, J. Rodríguez-Carvajal, A. Stunault, E. Ressouche, T. C. Hansen, M. T. Fernández-Díaz, M. R. Johnson, H. Fuess, H. Ehrenberg, Y. Sakurai, M. Itou, B. Gillon, T. Wolf, J. A. Rodríguez-Velamazan, and J. Sánchez-Montero, Experimental magnetic form factors in $Co_3V_2O_8$: A combined study of *ab initio* calculations, magnetic Compton scattering, and polarized neutron diffraction, Phys. Rev. B **79**, 094417 (2009).

[24] M. Ramazanoglu, C. P. Adams, J. P. Clancy, A. J. Berlinsky, Z. Yamani, R. Szymczak, H. Szymczak, J. Fink-Finowicki, and B. D. Gaulin, Spin waves in the ferromagnetic ground state of the kagome staircase system $Co_3V_2O_8$, Phys. Rev. B **79**, 024417 (2009).

[25] N. R. Wilson, O. A. Petrenko, G. Balakrishnan, P. Manuel, and B. Fak, Magnetic excitations in the kagomé staircase compounds, J. Magn. Magn. Mater. **310**, 1334 (2007).

[26] K. Fritsch, G. Ehlers, K. C. Rule, K. Habicht, M. Ramazanoglu, H. A. Dabkowska, and B. D. Gaulin, Quantum phase transitions and decoupling of magnetic sublattices in the quasi-two-dimensional Ising magnet $Co_3V_2O_8$ in a transverse magnetic field, Phys. Rev. B **92**, 180404(R) (2015).

[27] J. S. Helton, N. P. Butch, D. M. Pajerowski, S. N. Barilo, and J. W. Lynn, Three-dimensional magnetism and the Dzyaloshinskii-Moriya interaction in S = 3/2 kagome staircase $Co_3V_2O_8$, Sci. Adv. **6**, eaay9709 (2020).

[28] N. R. Wilson, O. A. Petrenko, and G. Balakrishnan, Magnetic phase diagrams of the kagomé staircase compounds $Co_3V_2O_8$ and $Ni_3V_2O_8$, J. Phys.: Condens. Matter **19**, 145257 (2007).

[29] Y. Yasui, Y. Kobayashi, M. Soda, T. Moyoshi, M. Sato, N. Igawa, and K. Kakurai, Successive magnetic transitions of the kagomé staircase compound $Co_3V_2O_8$ studied in various magnetic fields, J. Phys. Soc. Jpn. **76**, 034706 (2007).

[30] F. Yen, R. P. Chaudhury, E. Galstyan, B. Lorenz, Y. Q. Wang, Y. Y. Sun, and C. W. Chu, Magnetic phase diagrams of the kagomé staircase compound $Co_3V_2O_8$, Phys. B (Amsterdam, Neth.) **403**, 1487 (2008).

[31] J. S. Helton, Y. Chen, G. L. Bychkov, S. N. Barilo, N. Rogado, R. J. Cava, and J. W. Lynn, Evolution of the commensurate and incommensurate magnetic phases of the S = 3/2 kagome staircase $Co_3V_2O_8$ in an applied field, J. Phys.: Condens. Matter **24**, 016003 (2012).

[32] L. I. Vergara, J. Cao, L.-C. Tung, N. Rogado, F. Yen, Y. Q. Wang, R. J. Cava, B. Lorenz, Y.-J. Wang, and J. L. Musfeldt, Magnetoelastic coupling in magnetically frustrated $Co_3V_2O_8$, Phys. Rev. B **81**, 012403 (2010).

[33] N. Bellido, C. Martin, C. Simon, and A. Maignan, Coupled negative magnetocapacitance and magnetic susceptibility in a kagomé staircase-like compound $Co_3V_2O_8$, J. Phys.: Condens. Matter **19**, 056001 (2007)

[34] R. Szymczak, M. Baran, R. Diduszko, J. Fink-Finowicki, M. Gutowska, A. Szewczyk, and H. Szymczak, Magnetic field-induced transitions in geometrically frustrated $Co_3V_2O_8$ single crystal, Phys. Rev. B **73**, 094425 (2006).

[35] X. Zhao, J. C. Wu, Z. Y. Zhao, Z. Z. He, J. D. Song, J. Y. Zhao, X. G. Liu, X. F. Sun, and X. G. Li, Heat switch effect in an antiferromagnetic insulator $Co_3V_2O_8$, Appl. Phys. Lett. **108**, 242405 (2016).

[36] E. E. Sauerbrei, R. Faggiani, and C. Calvo, Refinement of the crystal structure of $Co_3V_2O_8$ and $Ni_3V_2O_8$ Acta. Crystallogr. Sect. B **29**, 2304 (1973).

[37] A. M. Tishin, in *Handbook of Magnetic Materials*, edited by K. H. J. Buschow (North-Holland, Amsterdam, 1999), Vol. 12.

[38] A. M. Tishin and Y. I. Spichkin, in *Condensed Matter Physics*, edited by J. M. D. Coey, D. R. Tilley, and D. R. Vij (IOP, Bristol, 2003), pp. 69–70.

[39] M. Patra, S. Majumdar, S. Giri, G. N. Iles, and T. Chatterji, Anomalous magnetic field dependence of magnetocaloric effect at low temperature in $Pr_{0.52}Sr_{0.48}MnO_3$ single crystal, J. Appl. Phys. **107**, 076101 (2010).

[40] H. Oesterreicher and F. T. Parker, Magnetic cooling near Curie temperatures above 300 K, J. Appl. Phys. **55**, 4334 (1984).

[41] M. D. Kuz'min, M. Richter, and A. M. Tishin, Field dependence of magnetic entropy change: Whence comes an intercept? J. Magn. Magn. Mater. **321**, L1 (2009).

[42] L. D. Landau and E. M. Lifshitz, *Electrodynamics of Continuous Media* (Butterworth-Heinemann, Oxford, 1999).

[43] T. Shang, A. Amon, D. Kasinathan, W. Xie, M. Bobnar, Y. Chen, A. Wang, M. Shi, M. Medarde, H. Q. Yuan, and T. Shiroka, Enhanced *Tc* and multiband superconductivity in the fully-gapped $ReBe_{22}$ superconductor, New J. Phys. **21**, 073034 (2019).

[44] R. Kumar and A. Sundaresan, Antisite disorder driven cluster glass state and colossal magnetoresistance in $MnSb_2Se_4$, Phys. Rev. B **106**, 134423 (2022).

[45] S. Chatterjee, P. Dutta, S. Giri, S. Majumdar, S. Sadhukhan, S. Kanungo, S. Chatterjee, M. M. Patidar, G. S. Okram, and V. Ganesan, Glassy magnetic state and negative temperature coefficient of resistivity in $Mn_{3+\delta}In$, Phys. Rev. B **102**, 214443 (2020).

[46] A. Banerjee, J. Sannigrahi, S. Giri, and S. Majumdar, Magnetization reversal and inverse exchange bias phenomenon in the ferrimagnetic polycrystalline compound Er_2CoMnO_6, Phys. Rev. B **98**, 104414 (2018).

[47] M. Das, P. Sarkar, and P. Mandal, Non-Griffiths-like cluster formation in the double-perovskite Gd_2CoMnO_6: Evidence from critical behavior, Phys. Rev. B **101**, 144433 (2020).

[48] E. Palacios, J. A. Rodríguez-Velamazán, M. Evangelisti, G. J. McIntyre, G. Lorusso, D. Visser, L. J. deJongh, and L. A. Boatner, Magnetic structure and magnetocalorics of $GdPO_4$, Phys. Rev. B **90**, 214423 (2014).

[49] M. Patra, K. De, S. Majumdar, and S. Giri, Multifunctionality attributed to the self-doping in polycrystalline $La_{0.9}MnO_3$: Coexistence of large magnetoresistance and magnetocaloric effect, Appl. Phys. Lett. **94**, 092506 (2009).

[50] M. Das, S. Roy, N. Khan, and P. Mandal, Giant magnetocaloric effect in an exchange-frustrated $GdCrTiO_5$ antiferromagnet, Phys. Rev. B **98**, 104420 (2018).

[51] K. Dey, A. Indra, S. Majumdar, and S. Giri, Cryogenic magnetocaloric effect in zircon-type RVO_4 (R = Gd, Ho, Er, and Yb), J. Mater. Chem. C **5**, 1646 (2017).

[52] A. Hadded, J. Massoudi, S. Gharbi, E. Dhahri, A. Tozri, and M. R. Berber, Study of physical properties of a ferrimagnetic spinel $Cu_{1.5}Mn_{1.5}O_4$: Spin dynamics, magnetocaloric effect and critical behavior, RSC Adv. **11**, 25664 (2021).

[53] K. A. Gschneidner, Jr., V. K. Pecharsky, and A. O. Tsokol, Recent developments in magnetocaloric materials, Rep. Prog. Phys. **68**, 1479 (2005).

[54] M.-H. Phan and S. C. Yu, Review of the magnetocaloric effect in manganite materials, J. Magn. Magn. Mater. **308**, 325 (2007).

[55] D. Benke, M. Fries, M. Specht, J. Wortmann, M. Pabst, T. Gottschall, I. Radulov, K. Skokov, A. I. Bevan, D. Prosperi, C. O. Tudor, P. Afiuny, M. Zakotnik, and O. Gutfleisch, Magnetic refrigeration with recycled permanent magnets and free rare-earth magnetocaloric La-Fe-Si, Energy Technol. **8**, 1901025 (2020).

[56] S. Mahana, U. Manju, and D. Topwal, Giant magnetocaloric effect in $GdAlO_3$ and a comparative study with $GdMnO_3$, J. Phys. D **50**, 035002 (2017).

[57] A. Midya, N. Khan, D. Bhoi, and P. Mandal, Giant magnetocaloric effect in antiferromagnetic $DyVO_4$ compound, Phys. B (Amsterdam, Neth.) **448**, 43 (2014).

[58] S. Mukherjee, G. Manna, P. Saha, S. Majumdar, and S. Giri, Ferroelectric order with a linear high-field magnetoelectric coupling in $Na_2Co_2TeO_6$: A proposed Kitaev compound, Phys. Rev. Mater. **6**, 054407 (2022).

[59] A. Karmakar, K. Dey, S. Chatterjee, S. Majumdar, and S. Giri, Spin correlated dielectric memory and rejuvenation in multiferroic $CuCrS_2$, Appl. Phys. Lett. **104**, 052906 (2014).

[60] K. Dey, A. Karmakar, A. Indra, S. Majumdar, U. Rütt, O. Gutowski, M. v. Zimmermann, and S. Giri, Thermally assisted and magnetic field driven isostructural distortion of spinel structure and occurrence of polar order in $CoCr_2S_4$, Phys. Rev. B **92**, 024401 (2015).

[61] A. Indra, K. Dey, S. Majumdar, I. Sarkar, S. Francoual, R. P. Giri, N. Khan, P. Mandal, and S. Giri, Magnetoelectric memory in reentrant frozen state and considerable ferroelectricity in the multiferroic spin-chain compound Sm_2BaNiO_5, Phys. Rev. B **95**, 094402 (2017).

[62] J. K. Dey, S. Majumdar, and S. Giri, Coexisting exchange bias effect and ferroelectricity in geometrically frustrated $ZnCr_2O_4$, J. Phys.: Condens. Matter **30**, 235801 (2018).

[63] J. K. Dey, A. Chatterjee, A.-C. Dippel, O. Gutowski, M. v. Zimmermann, S. Majumdar, and S. Giri, Rhombohedral distortion-driven ferroelectric order and exchange bias effect in geometrically frustrated $ZnFe_2O_4$, Phys. Rev. Mater. **5**, 014410 (2021).

[64] T. D. Sparks, M. C. Kemei, P. T. Barton, R. Seshadri, E.-D. Mun, and V. S. Zapf, Magnetocapacitance as a sensitive probe of magnetostructural changes in $NiCr_2O_4$, Phys. Rev. B **89**, 024405 (2014).

[65] N. Mufti, A. A. Nugroho, G. R. Blake, and T. T. M. Palstra, Magnetodielectric coupling in frustrated spin systems: The spinels MCr_2O_4 (M = Mn, Co and Ni), J. Phys.: Condens. Matter **22**, 075902 (2010).

[66] T. Kimura, S. Kawamoto, I. Yamada, M. Azuma, M. Takano, and Y. Tokura, Magnetocapacitance effect in multiferroic $BiMnO_3$, Phys. Rev. B **67**, 180401(R) (2003).

[67] T. N. M. Ngo, U. Adem, and T. T. M. Palstra, The origin of thermally stimulated depolarization currents in multiferroic $CuCrO_2$, Appl. Phys. Lett. **106**, 152904 (2015).

[68] N. Terada, Y. S. Glazkova, and A. A. Belik, Differentiation between ferroelectricity and thermally stimulated current in pyrocurrent measurements of multiferroic MMn$_7$O$_1$2 (M = Ca, Sr, Cd, Pb), Phys. Rev. B **93**, 155127 (2016).

[69] R. Chen and Y. Kirsh, *Analysis of Thermally Stimulated Process* (Pergamon, New York, 1981).

[70] T. Kimura, Y. Sekio, H. Nakamura, T. Siegrist, and A. P. Ramirez, Cupric oxide as an induced-multiferroic with high-T_C, Nat. Mater. **7**, 291 (2008).

[71] K. Dey, A. Indra, S. Mukherjee, S. Majumdar, J. Strempfer, O. Fabelo, E. Mossou, T. Chatterji, and S. Giri, Natural ferroelectric order near ambient temperature in the orthoferrite $HoFeO_3$, Phys. Rev. B **100**, 214432 (2019).

[72] X. Moya, S. Kar-Narayan, and N. D. Mathur, Caloric materials near ferroic phase transitions, Nat. Mater. **13**, 439 (2014).

[73] K. Dey, A. Indra, A. Karmakar, and S. Giri, Multicaloric effect in multiferroic sulpho spinel MCr_2S_4 (M=Fe, Co), J. Magn. Magn. Mater. **498**, 166090 (2020).

[74] C. Dhanasekhar, A. K. Das, and A. Venimadhav, Multiple caloric effects in geometrically frustrated "114" $CaBaCo_4O_7$ cobaltite, J. Magn. Magn. Mater. **418**, 76 (2016).

[75] J. Krishna Murthy and A. Venimadhav, Multicaloric effect in multiferroic Y_2CoMnO_6, J. Phys. D **47**, 445002 (2014).

[76] S. Kesari, R. Rao, M. K. Gupta, R. Mittal, and G. Balakrishnan, Symmetries of modes in $Ni_3V_2O_8$: Polarized Raman spectroscopy and ab initio phonon calculations, J. Raman Spectrosc. **50**, 587 (2019).

[77] Y. S. Seo, S. H. Kim, and J. S. Ahn, Determination of the local symmetry and the multiferroic-ferromagnetic crossover in $Ni_{3-x}Co_xV_2O_8$ by using Raman scattering spectroscopy, J. Korean Phys. Soc. **62**, 116 (2013).

[78] K. Dey, S. Majumdar, and S. Giri, Ferroelectricity in spiral short-range-ordered magnetic state of spinel $MnCr_2O_4$: Significance of topological frustration and magnetoelastic coupling, Phys. Rev. B **90**, 184424 (2014).

[79] A. Indra, K. Dey, J. K. Dey, S. Majumdar, U. Rütt, O. Gutowski, M. v. Zimmermann, and S. Giri, CrO_4 distortion-driven ferroelectric order in (R, Y)CrO_4 (R = Sm, Gd, and Ho): A new family of multiferroics, Phys. Rev. B **98**, 014408 (2018).

[80] A. Indra, K. Dey, A. Midya, P. Mandal, O. Gutowski, U. Rütt, S. Majumdar, and S. Giri, Magnetoelectric coupling and exchange bias effects in multiferroic $NdCrO_3$, J. Phys.: Condens. Matter **28**, 166005 (2016).

[81] A. Chatterjee, J. K. Dey, S. Majumdar, A. C. Dippel, O. Gutowski, M. v. Zimmermann, and S. Giri, Tuning of multiferroic order with Co doping in $CuCr_2O_4$: Interplay between structure and orbital order, Phys. Rev. Mater. **3**, 104403 (2019).

[82] J. K. Dey, A. Chatterjee, S. Majumdar, A. C. Dippel, O. Gutowski, M. v. Zimmermann, and S. Giri, Ferroelectric order associated with ordered occupancy at the octahedral site of the inverse spinel structure of multiferroic $NiFe_2O_4$, Phys. Rev. B **99**, 144412 (2019).

[83] B. J. Campbell, H. T. Stokes, D. E. Tanner, and D. M. Hatch, *ISODISPLACE:* a web-based tool for exploring structural distortions, J. Appl. Crystallogr. **39**, 607 (2006).